Open Ceramics 16 (2023) 100446

Contents lists available at ScienceDirect

Open Ceramics

journal homepage: www.sciencedirect.com/journal/open-ceramics

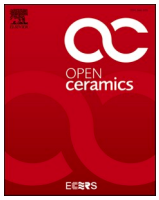

Novel microporous MgO-based high-temperature thermal insulator

Rafael Salomão [a,*], Leandro Fernandes [a], Luiz Carlos Simão [b]

[a] São Carlos School of Engineering, University of São Paulo, Materials Engineering Department, Avenida Trabalhador São-carlense 400, São Carlos, SP, Brazil
[b] Fibertechnic Ltda, Valinhos, SP, Brazil

ARTICLE INFO

Handling Editor: Dr P Colombo

Keywords:
Microporous MgO
Thermal insulator
Energy saving

ABSTRACT

This paper addresses the development of a novel microporous MgO-based (MPMB) thermal insulator whose temperature-resistant microporous structure was engineered for the introduction of controlled packing flaws amongst their highly asymmetric and porous particles during compacting by uniaxial pressing. Hard-burnt MgO, dolomite, and TiO_2 particles were dry-mixed with expanded aluminum phyllosilicate and fibers before being sprayed with a colloidal silica dispersion. The mixture was uniaxially pressed as 400 × 100 × 20 mm boards and dried at 120 °C. Samples were thermally treated at different temperatures (120-1100 °C) for the evaluation of their physical properties (compression strength, rigidity, permanent dimensional thermal variation, solid density, total porosity, pore diameter distribution, and thermal conductivity), crystalline phases, and microstructure. The microporous microstructure generated during pressing was not significantly affected by thermal treatments up to 1100 °C and the samples' thermal conductivity, total porosity, and compression strength varied between 0.20 and 0.14 W (m K)$^{-1}$, 54–56%, and 29-15 MPa in the 200-1000 °C temperature range.

1. Introduction

Microporous refractory ceramics are effective barriers against undesired heat exchange at temperatures above 300 °C due to a useful combination of characteristics [1–8]. Their microstructure contains pores with a designed balance between volumetric fraction (50–80%), diameter distribution (0.5–5 μm), geometry, and degree of interconnection (ideally isolated spheres) [9–16] Taylor-made to scatter and block different types of heat waves. On the other hand, the solid ceramic phase surrounding such functional pores shows significant corrosion and densification resistance for avoiding microstructure changes, extending materials' service life, and preventing maintenance operations [17–24] In comparison to ceramic fiber-based insulators, microporous refractories show straightforward manufacturing and installation and superior thermo-mechanical properties and produce no hazardous particulate debris [25–31]. They also show lower thermal conductivity and diffusivity above 700 °C at which heat loss by infrared radiation becomes the dominant mechanism [32–40].

The fabrication of microporous refractories usually involves the use of a porogenic additive for the production of a large number of pores with the desired characteristics and a densification-resistant mechanism for preventing microstructure and properties changes during long periods of use at high temperatures [41–46]. Based on such a strategy, several studies developed combinations of raw materials and processing techniques, resulting in microporous ceramic structures. As an example, the addition of excess of water [47–49], ice templating [50–52], organic particles (e.g., starch [53–55], chitosan [56], alginic salt [57], and synthetic polymers [26,27,31,41,58–62]), or foams [28,33,40,63–68] to stable particles' suspension produces cellular ceramics whose total porosity levels can be as high as 90%. On the other hand, aqueous dispersions of α-Al_2O_3 containing solid inorganic porogenic agents (α-$Al(OH)_3$ [18,21,56,69–71], SiO_2 [44,47,72–76], $Mg(OH)_2$ [21,23,29,77–81], $CaCO_3$ [46,82–84]), and binders (ρ-Al_2O_3, calcium aluminate cement [85,86]) form castable systems which evolve to microporous refractories of α-Al_2O_3, $Al_9Si_3O_{13}$, $MgAl_2O_3$, and $CaAl_{12}O_{19}$ after sintering, respectively. Since such compounds are intrinsically densification-resistant, they are good candidates for applications that require long exposures to high temperatures [87].

All aforementioned porogenic mechanisms share a common characteristic, i.e., their activation requires a certain level of heating to generate pores and achieve minimal handling strength. Consequently, careful heating schedules are necessary for preventing cracks related to volatile withdrawal [41,49,58,59,85] and the level of thermal insulation is not as high as possible in the initial stages. To overcome such drawbacks, this study investigated the use of a different porogenic strategy based on the generation of controlled packing flaws amongst refractory

* Corresponding author.
E-mail address: rsalomao@sc.usp.br (R. Salomão).

https://doi.org/10.1016/j.oceram.2023.100446
Received 27 June 2023; Received in revised form 28 August 2023; Accepted 29 August 2023
Available online 30 August 2023

Table 1
Characteristics of the raw materials employed to produce the microporous MgO-based (MPMB) composition tested.

Characteristics		Raw materials					
		Hard-burnt magnesia	Calcitic dolomite	Expanded aluminum phyllosilicate	TiO_2	Colloidal silica	Polymeric fibers
[a] Composition (wt%)	MgO	98.3	42.4	15.8	0.00	0.00	–
	CaO	0.72	54.7	7.00	0.00	0.00	–
	Al_2O_3	0.18	0.35	26.4	0.00	0.00	–
	SiO_2	0.18	1.70	43.3	0.00	99.0	–
	Na_2O	0.16	0.33	4.70	0.01	1.00	–
	K_2O	0.25	0.20	0.80	0.00	0.00	–
	Fe_2O_3	0.21	0.32	2.00	0.00	0.00	–
	TiO_2	0.00	0.00	0.00	99.9	0.00	–
Average diameter (μm)		6.3	28.9	202	0.08	0.02	25 μm
Surface area ($m^2.g^{-1}$)		1.2	0.8	194	180	212	–
[b] Solid density ($g.cm^{-3}$)		3.5	2.8	1.9	4.2	2.1	0.99
Ratio at the MPMB (wt%)		74.8	4.5	10.0	0.6	10.0	0.1

[a] After calcination at 1000 °C for 5 h.
[b] after drying at 120 °C overnight.

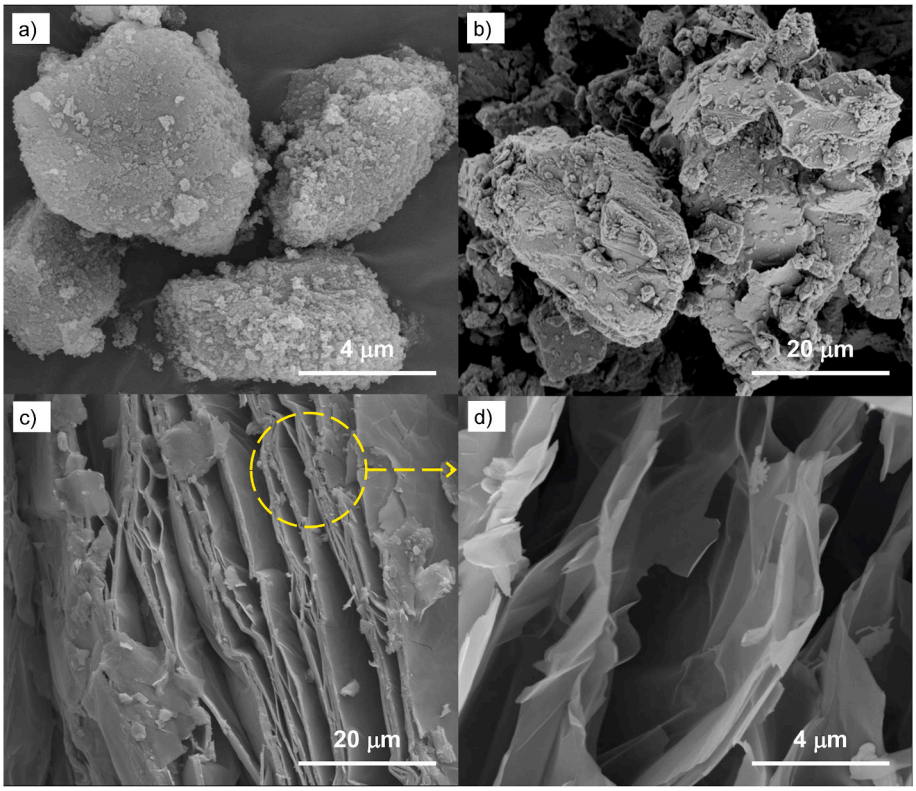

Fig. 1. SEM images of the as-received raw materials employed: a) hard-burnt MgO, b) calcareous dolomite, *c*-d) expanded aluminum silicate.

particles for the production of a microporous MgO-based (MPMB) thermal insulator. Mixtures of different MgO-based raw materials containing a significant fraction of intra-particle pores and aluminum-silicate-based-ones comprised of highly asymmetric particles were shaped as boards by uniaxial pressing assisted by a bonding spray of colloidal silica. Compared to the other porogenic methods presented, such a strategy showed energy-saving straightforward processing, since the structures produced require no previous thermal treatment to attain sufficient strength and porosity.

2. Experimental

Hard-burnt magnesia (α-MgO, RHI-Magnesita, Brazil), coarse calcitic dolomite ($(Mg.Ca)CO_3$. Ouro Branco, Brazil), polymeric fibers (Polypropylene, Fitesa, Brazil), expanded aluminum phyllosilicate ($(Mg,Fe^{2+},Fe^{3+})_3(Al,Si)_4O_{10}(OH)_2.4H_2O$, MSL, Brazil), and titanium dioxide (TiO_2, rutile, Synth, Brazil) were initially dry-mixed and sprayed with colloidal silica (30 wt% of solids, FO830, Nouryon, Brazil) before being shaped as 400 × 100 × 12 mm flat boards by uniaxial pressing (50 MPa, 60 s) (Table 1). The boards (Nanoxtherm, Fibertechnich, Brazil) were then dried overnight at 120 °C and sliced as 100 × 40 × 12 mm prisms, for measurements of total porosity and permanent thermal dimensional variation, and as 12 × 12 × 12 mm cubes, for cold crushing and drying tests.

The drying behavior of green humid freshly pressed samples of approximately 100 g was evaluated in tailor-made thermogravimetric equipment [85,86] that monitors temperature and mass changes of samples placed in an electric furnace every 10 s. The samples were heated up to 700 °C (2 °C.min^{-1} heating rate) and the instantaneous percent mass loss (W, wt%) and mass loss rate (dW/dT, wt%.°C^{-1}) were

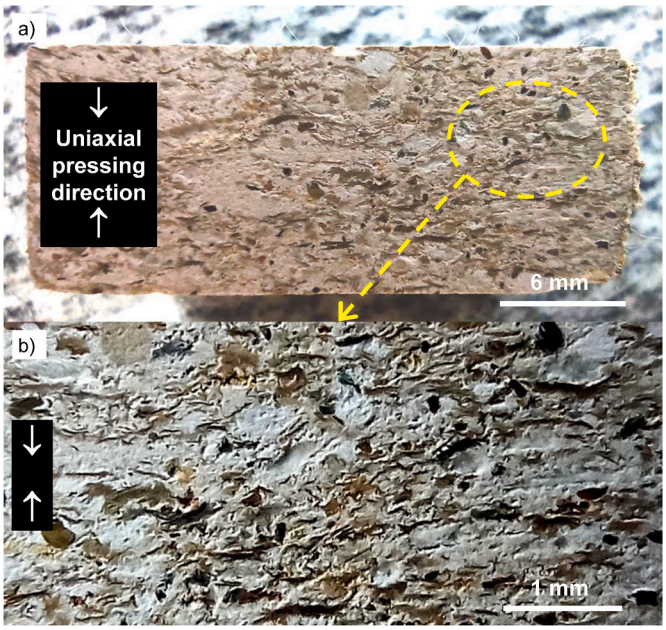

Fig. 2. Stereoscopic images of cross-section of the as-produced MPMB thermal insulator. White arrows indicate the direction of uniaxial pressing.

Table 2
Composition of the system (theoretical and after pressing and drying at 120 °C).

Oxides from raw materials	[a] Total composition of the system (wt%)		
	Theoretical (green-dried)	XRF (green-dried)	*EDS (green-dried, Fig. 3)*
MgO	77.0	74.4	78.2
CaO	3.70	4.51	3.20
Al_2O_3	2.80	3.90	2.10
SiO_2	14.4	15.5	14.8
Na_2O	0.70	0.89	1.10
K_2O	0.28	0.12	0.15
Fe_2O_3	0.38	0.21	0.18
TiO_2	0.74	0.47	0.27

[a] The carbon content from polymeric fibers and dolomite was not considered in this analysis.

calculated by Equations (1) and (2), respectively:

$$W = 100\% \times [(M_{Inicial} - M_{Inst}) \ / \ (M_{Inicial} - M_{Final})] \quad (1)$$

$$(dW/dT)_T = (W_{T+10} - W_{T-10}) \ / \ (T_{T+10} - T_{T-10}) \quad (2)$$

where $M_{Inicial}$ is the sample's mass after casting and before the curing period, M_{Inst} is the instantaneous mass for a certain temperature (T), and M_{Final} is the mass at the end of heating [21,41,58,59,86–89].

Samples for the evaluation of physical properties remained at 120 °C ± 1 °C for 24 h. Such conditions also maximize the binding action of colloidal silica and reduce the risks of damage by MgO excessive hydroxylation and explosive spalling during the first heat-up [88,89]. After drying, the samples were thermally treated at 200–1100 °C for 3 h (1 °C.min^{-1} up to 400 °C, 1 h; 2 °C.min^{-1} up to maximum temperature, 3 h hold; 5 °C.min^{-1} cooling rate up to 800 °C and 10 °C.min^{-1} down to room temperature).

Dried green (G) and sintered (St) samples were measured (length, L, width, W, and thickness, T, in cm) and weighted (M, g). Their total porosity (TP, %) was calculated by Equation (3) using solid density (ρ) values attained by Helium pycnometry in equivalent compositions after grinding ($D_{Particle} \leq 100$ μm).

$$TP\ (\%) = 100\% \times \{1 - [(M) \ / \ (L \times W \times T \times \rho)]\} \quad (3)$$

Equation (4) calculated the samples' permanent thermal dimensional variation (TDV, %):

$$TDV\ (\%) = 100 \times [(L_{St} - L_G) \ / \ L_G] \quad (4)$$

Their compression strength (CS, MPa, Equation 10) was calculated by Equation 5 and an MTS 810 TestStar II tensile tester at a 2 N s^{-1} loading rate:

$$CS\ (MPa) = F \ / \ (L \times W) \quad (5)$$

where F (in N) is the maximum load before rupture. Each value of total porosity, compression strength, and permanent thermal dimensional variation is the average result of the testing of five samples, whereas the error bars represent their standard deviation.

The samples' thermal conductivity was measured by calorimetric method (ASTM C-201, "Standard Test Method for Thermal Conductivity of Insulating Firebrick"), in the 200-1000 °C temperature range for 100 × 40 × 20 mm boards previously fired for 5 h at each particular temperature [10–13,17,25,36,37].

Samples' pore size distribution (green-dried, and sintered at 1000 °C and 1100 °C) was assessed by mercury intrusion porosimetry (PoreMaster 33, Quantochrome Instruments, USA; mercury surface tension equal to 0.480 N.m-1; 130° contact angle and pressure applied to range between 0.0014 and 210 MPa).

The phases and microstructures formed after each thermal treatment were evaluated in equivalent samples by X-ray diffraction (crushed samples, $D_{Part} < 100$ μm, Rotaflex RV 200B, Rigaku-Denki Corp., Japan, λ = 0.14506 nm, in the 2θ range from 10 to 70° at a 0.5°.min^{-1} scan rate, against standard JCPDS files), X-ray dispersive spectroscopy (Shimadzu, EDX 720, Japan, after calcination at 1000 °C for 5 h), stereo optical microscopy (Zeiss, SteREO Discovery V8, with a camera for image acquisition AxioCam ERc5s, Germany), and scanning electron microscopy (fractured surfaces, FEI 7500F, Netherlands, equipped with an energy dispersive spectrometer, Apollo, EDAX, USA, for EDS mapping), respectively.

3. Results and discussion

3.1. Raw materials and green-dried samples

The raw materials employed in this study showed significant differences in their microstructure. Whereas hard-burnt MgO (Fig. 1a) and dolomite (Fig. 1b) particles are coarse and irregularly shaped, the expanded phyllosilicate ones (Fig. 1c and d) displays a typical highly asymmetric lamellar geometry with a certain level of intra-particle porosity. The submicrometric pores of hard-burnt MgO particles originated during the calcination of magnesite ($MgCO_3$) [89] and those of dolomite resemble cracks and fractured surfaces created due to milling. The phyllosilicate ones contain inter-lamellar voids longer than 20 μm and thicker than 1–5 μm formed due to partial dehydroxylation processes occurred under hydrothermal conditions before extraction [2,3,90,91].

The total composition of the flat boards attained after pressing and drying at 120 °C (Fig. 2a and b) contained MgO, SiO_2, and CaO as their major components (77 wt%, 14.4 wt%, ad 3.7 wt%, respectively), and Al_2O_3 (2.8 wt%), Na_2O (0.7 wt%), K_2O (0.3 wt%), Fe_2O_3 (0.4 wt%), and TiO_2 (0.7 wt%) in smaller quantities as impurities from de main raw materials (except TiO_2, which was intentionally added) (Table 2). They exhibited a two-phase microstructure (Fig. 3a) with different populations of pores (Fig. 4a). The follicular phase comprises lamellar particles of expanded phyllosilicate (Fig. 3b and 5a) aligned perpendicularly to the pressing direction and their large quantity of inter-lamellar voids (detailed in Fig. 1d) corresponds to the population of pores whose diameters range between 2 and 8 μm. On the other hand, the granular phase (Fig. 3c) surrounds the follicular one and contains irregular thicker particles of MgO, dolomite, and thin crystals of xonolite

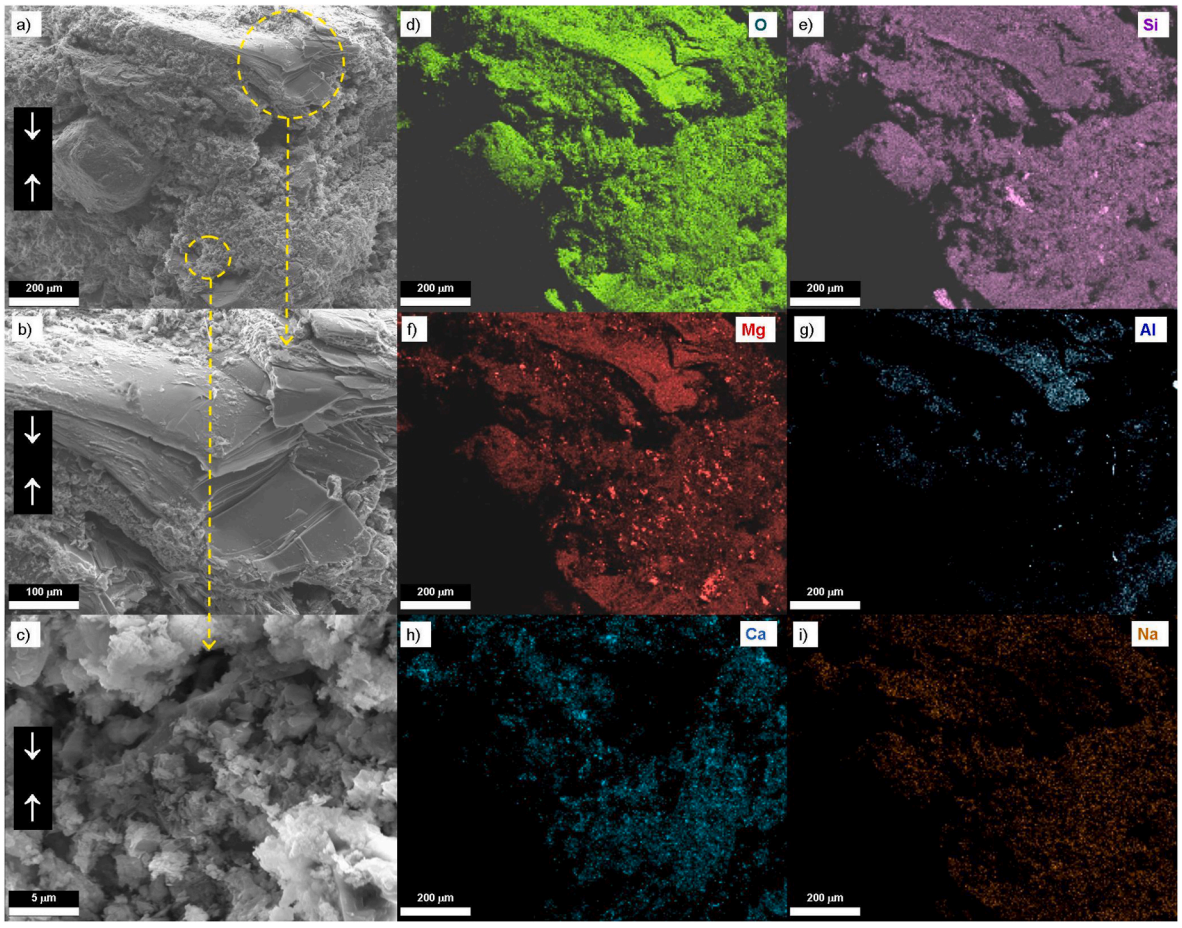

Fig. 3. SEM images detailing a) overall two-phase microstructure containing b) follicular and c) granular regions and their elemental composition (d) oxygen, e) silicon, f) magnesium, g) aluminum, h) calcium, i) sodium). White arrows indicate the direction of uniaxial pressing. (For interpretation of the references to colour in this figure legend, the reader is referred to the Web version of this article.)

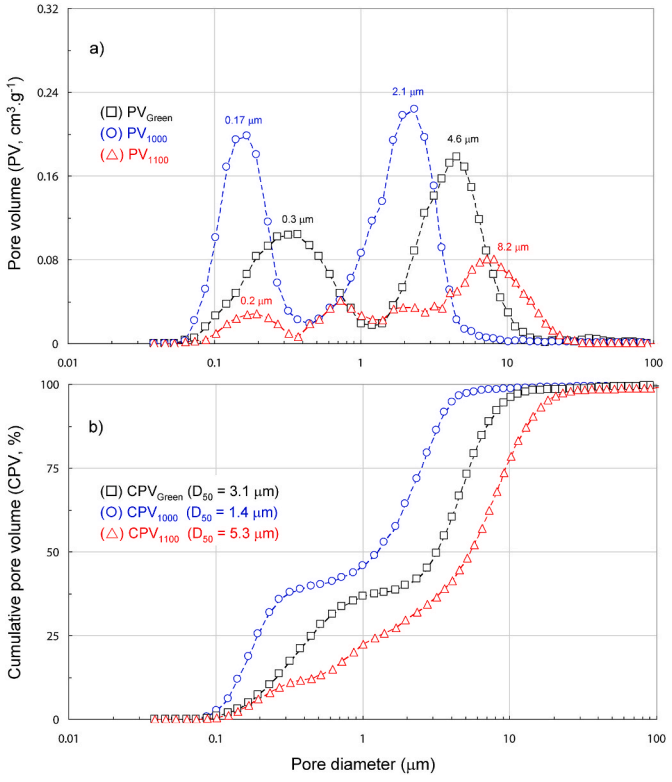

Fig. 4. a) Discrete and b) cumulative pore size distribution for MPMB samples thermally treated at 120 °C, 1000 °C, and 1100 °C.

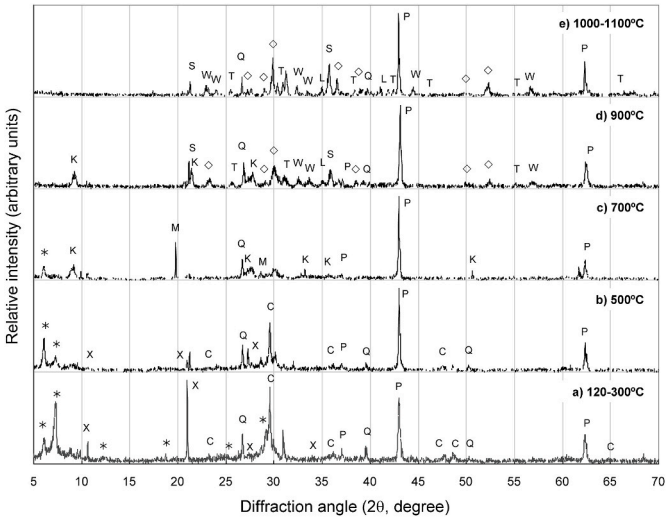

Fig. 5. XRD patterns for MPMB samples thermally treated from 120 °C up to 1100 °C. List of symbols: P = Periclase (α-MgO, PDF = 1–1235); C = Calcite ($CaCO_3$, PDF = 1–837); ✱= Magnesium aluminum iron silicate hydrate ($(Mg,Fe^{2+},Fe^{3+})_3(Al,Si)_4O_{10}(OH)_2.4H_2O$, PDF = 2.21); X = Xonolite ($Ca_6Si_6O_{17}\cdot(OH)_2$, PDF = 2–598); Q = Quartz (SiO_2, PDF = 2–471); K = Magnesian muscovite ($(K,Mg,Al)Si_4O_{10}(OH)_2$, PDF = 21.993); M = Potassium aluminum silicate hydroxide hydrate ($KAl_4(SiAl)_8O_{20}(OH)_4.5H_2O$, PDF = 7–330); W = Wollastonite ($CaSiO_3$, PDF = 2–689); L = Lime (CaO, PDF = 17–912); ⋄ = β-Wollastonite ($CaSiO_3$, PDF = 3–626); S= Cristobalite (SiO_2, PDF = 2–278); T = Brokite (TiO_2, 29–1360).

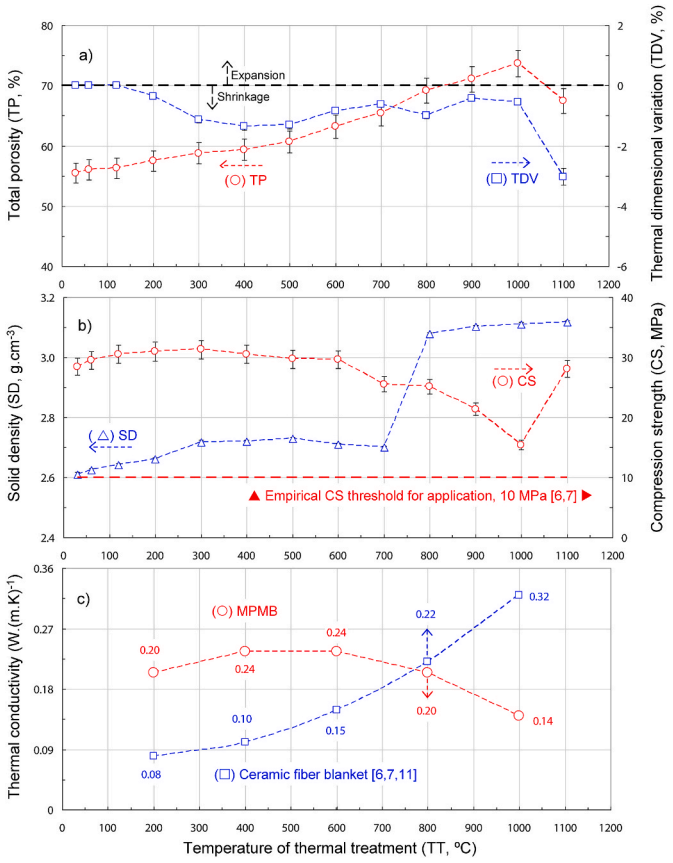

Fig. 6. Evolution of physical properties of microporous MgO-based (MPMB) thermal insulator with thermal treatment up to 1100 °C: a) total porosity (TP) and thermal dimensional variation (TDV), b) solid density (SD) and compression strength (CS), c) thermal conductivity (typical thermal conductivity results for ceramic fiber blocks are also shown as a reference [6,7,11]).

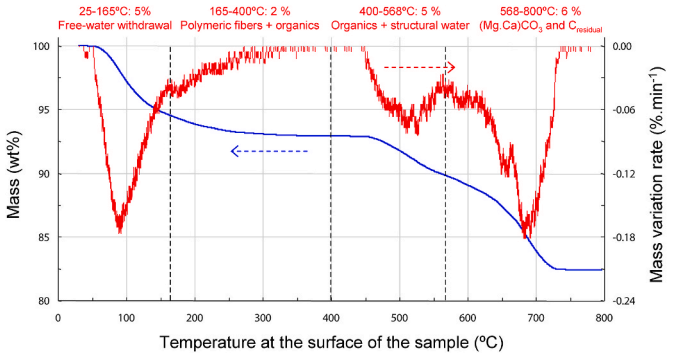

Fig. 7. Mass loss and mass loss rate versus sample temperature behavior for MMB structures.

($Ca_6Si_6O_{17}$·$(OH)_2$) (Fig. 5a). Whereas xonolite crystals were formed *in situ* due to the reaction between colloidal silica and calcium sources [92–94], the other phases present were periclase, from hard-burnt MgO, and calcite and quartz (as an impurity), from dolomite. These particles' inner pores and the packing flaws amongst them comprised the second population of thin pores (0.3–0.5 μm). The elemental analysis (Fig. 3d–i) also revealed part of the colloidal silica particles formed a continuous non-crystalline coating over all surfaces available (Fig. 3e), explaining the high concentration of sodium, which is an impurity in colloidal silica, in the finer parts of the granular phase (Fig. 3i).

Interestingly, although the major component of the structure is hard-burnt MgO and a significant amount of water was added to the composition during mixing and pressing, no substantial evidence of Mg $(OH)_2$ formation (e.g., volumetric expansion, cracks, or crumbling) was observed during or after drying. Such an unusual effect is related to the fact colloidal silica and other amorphous silica sources exert a strong anti-hydroxylation action upon MgO particles due to the formation of a thin and highly stable protective coating of magnesium silicate hydroxide hydrate [95–97].

Non-structural thermal insulators, such as blocks of compacted ceramic fibers, loose-fill insulators, and fired-chamotte bricks typically present total porosity, compression strength, and thermal conductivity levels ranging between 30 and 50%, 1–10 MPa, and lower than 0.2 W $(m\ K)^{-1}$, respectively [6]. Green-dried samples displayed similar total porosity (54%, Fig. 6a) and significantly higher strength before any thermal treatment (28 MPa, Fig. 6b). Such an unusual result is related to two effects. First, the gelling of colloidal silica during curing and drying produced tight connections amongst particles at the same time no hydroxylated compound was produced to fill the inter-particle voids [67,98,99]. Second, the large content of small intra-particle pores (3.1 μm, Fig. 4b) caused no deleterious effects on strength [70]. Another interesting aspect is, differently from other studies in which porogenic mechanisms were triggered by dehydroxylation or burnout reactions [18,21,23,28,33,44,46,53,61], the pores observed at the cross-section of the MMB structure resulted from controlled packing flaws generated during pressing. The technological implication of such results is the material behaves as a thermal insulator after the early drying stages, as indicated by the low level of thermal conductivity measured at 200 °C (0.2 W $(m\ K)^{-1}$) (Fig. 3c) [6–8].

3.2. Thermal treatments up to 800 °C

During the initial heating up to 400 °C, the freshly pressed samples showed a 5% increase in total porosity followed by 1.7% shrinkage and up to 7 wt% mass loss (Fig. 6a and b and 7). Such a behavior is a microstructure accommodation caused by free-water withdrawal from colloidal silica and burnout of organic matter from phyllosilicate and polymeric fibers [41,49,58,59]. In the 400-568 °C temperature range, the final withdrawal of residues of organic matter and structural water from phyllosilicate preceded the decarbonation of dolomite and burnout of other carbonaceous residues from 568 °C up to 700 °C. The corresponding enhancement in solid density and total porosity and the formation of cracks along the pressing direction due to the release of water vapor and other volatiles (Fig. 8a and b) led to slightly lower compression strength levels (Fig. 6b). During the thermal treatment,

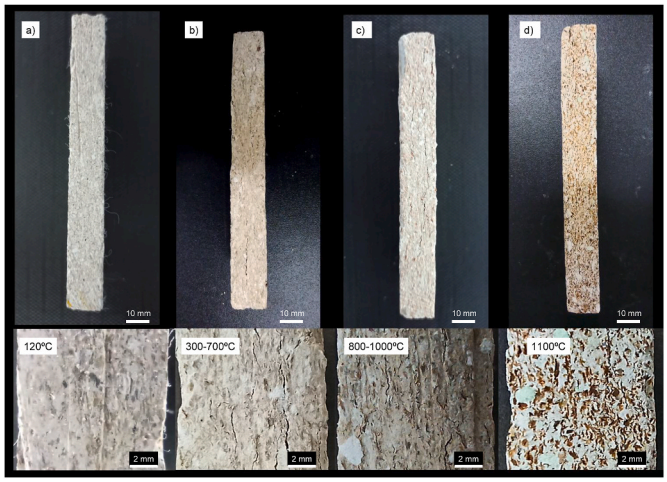

Fig. 8. Stereoscopic images of samples of MPMB thermal insulator thermally treated at different temperatures (a) 120 °C, b) 300-700 °C, c) 800-900 °C, and d) 1000-1100 °C) detailing the lamination cracks formed during heating and the surface aspect.

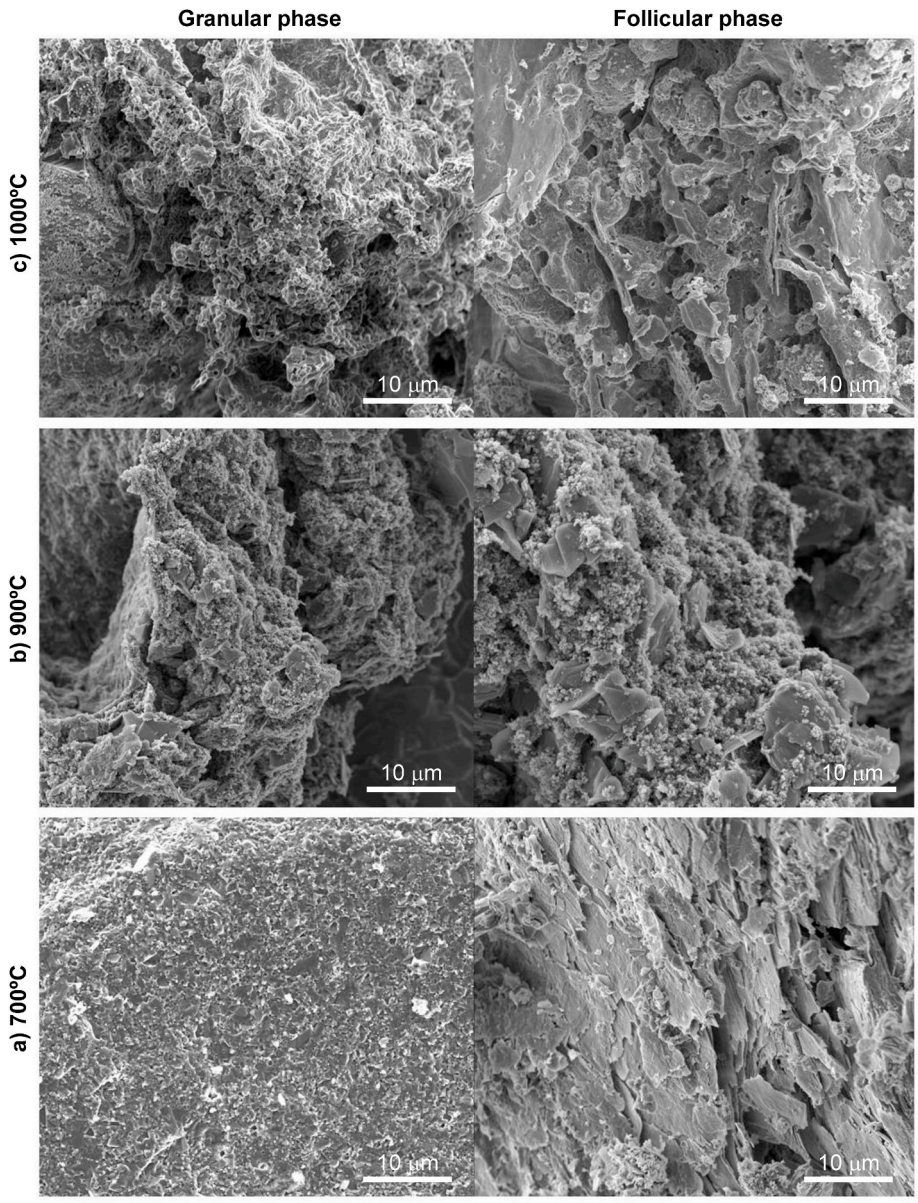

Fig. 9. SEM images of the cross-section of MPMB thermal insulator thermally treated at different temperatures (a) 700 °C, b) 900 °C, and c) 1100 °C) detailing granular and follicular phases.

periclase remained the main crystalline phase, whereas CaO from dolomite combined with quartz (SiO_2) forming wollastonite (Ca_2SiO_4) (Fig. 5b and c). Concomitantly, the expanded phyllosilicate turned into meta-phyllosilicate (similar structure with no structural water, $(Mg,Fe^{3+})_3(Al,Si)_4O_{10}$)) and combined with MgO forming magnesian muscovite ($(K,Mg,Al)Si_4O_{10}$) [100,101].

An intense increase in solid density and crack formation (Fig. 8c) was observed between 700 and 800 °C was related to a collapse of multi-oxide sheets in phyllosilicate and muscovite, since no significant evidence of liquid phase was detected in the microstructure (Fig. 9a). Interestingly, up to 800 °C, the permanent thermal shrinkage (TDV, Fig. 6a) remained below 2 wt%, which is an important technological parameter regarding the structural integrity of the thermal insulator lining during long periods of service [6,7].

3.3. Thermal treatments above 800 °C

Above 800 °C, both solid density and linear shrinkage stabilized, whereas total porosity continuously increased up to 1000 °C, reducing compression strength (Fig. 6a and b). Such behavior was attributed to the formation of a small portion of liquid compounds based on the SiO_2–Na_2O–CaO system [102] amongst partially sintered MgO and CaO coarse particles. The rigidity of the structure prevented shrinkage and pores' growth (Figs. 4 and 9b-c). Two other interesting effects were observed for samples treated at 1000 °C. First, the boundaries between follicular and granular phases became less defined (Fig. 10a and b). Due to the high atomic mobility introduced by the liquid phase, the original elements of each phase were mixed throughout the entire microstructure (Fig. 10c–h). Secondly, a significant reduction in thermal conductivity followed the microstructure changes observed between 800 and 1000 °C, differing from the behavior of ceramic-fibers blankets, which showed higher thermal conductivity as temperature increased (Fig. 6c) [6,7,11,15,17,25]. Such behavior indicates refractory structures containing micropores (1.4 μm, Fig. 4b) can scatter infrared electromagnetic heat waves, which are the dominant heat transfer mechanism above 600 °C [5–7,10,13–16]. Moreover, the small initial content of TiO_2 (Fig. 5d and e) may have exerted a certain opacifying effect on infrared radiation, blocking its propagation [11,15,36–40,74]. In the

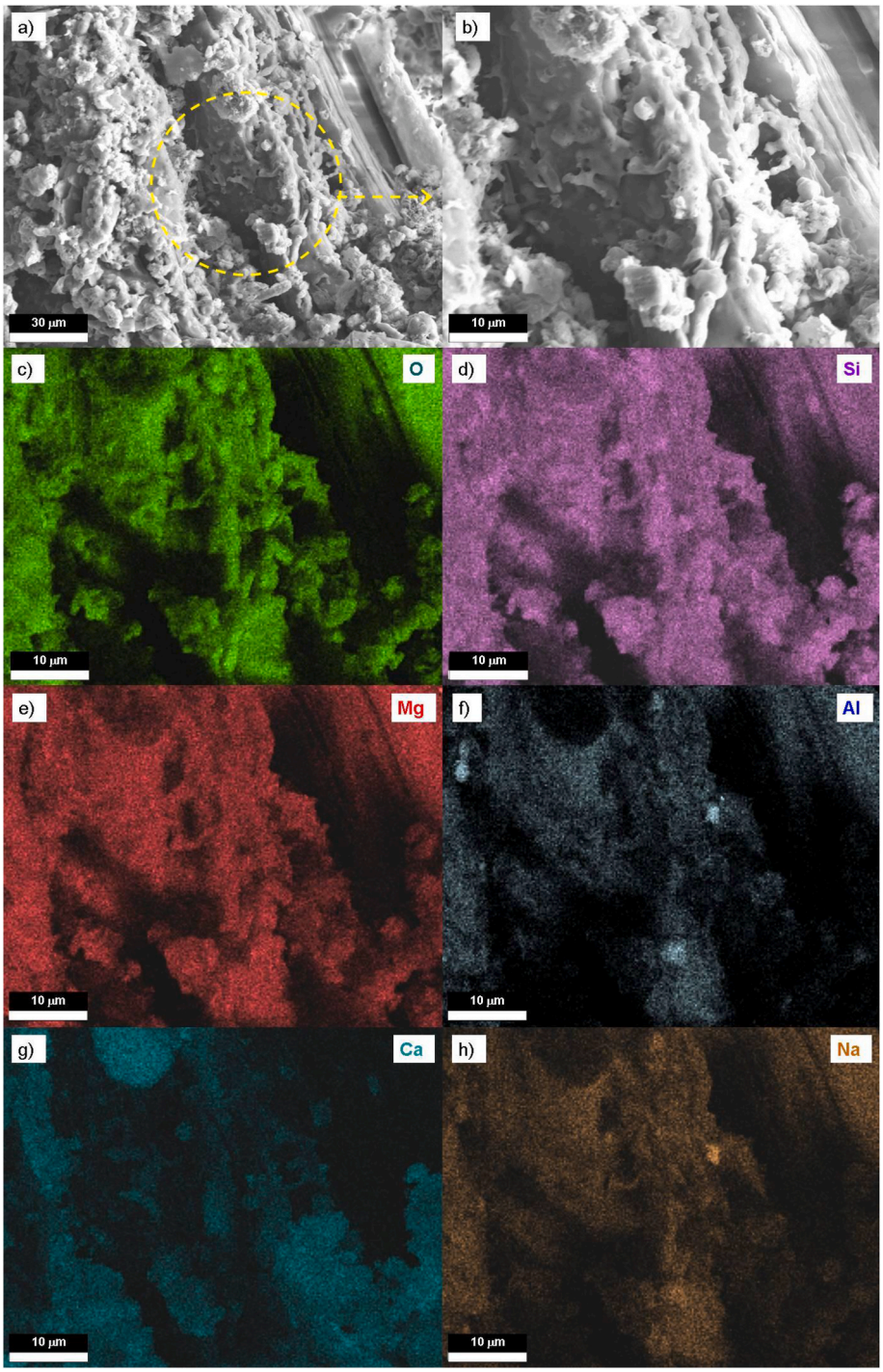

Fig. 10. SEM images of the cross-section of MPMB thermal insulator thermally treated at 1000 °C detailing the interface between follicular and granular phases.

same temperature range, fiber blankets were less effective in block heat flow due to their excessive pore fraction, which increased the mean free path for photons throughout the structure [11,15,25].

Above 1000 °C, the formation of larger quantities of liquid phase led to significant shrinkage levels and total porosity reduction (Fig. 6a). Although those samples became stronger (Fig. 6b), they experienced a structural collapse (Fig. 8d). The excessive shrinkage (Fig. 11a and b) and the presence of liquid phase promoted the formation of lamination voids (Fig. 11c and d) that increased the average pore size (5.3 µm, Fig. 4b), suggesting 1100 °C should be the maximum temperature of use.

4. Conclusions

This study focused on the characterization of a microporous MgO-based thermal insulator (MPBM) developed by a novel porogenic approach. During uniaxial pressing of flat boards, the presence of highly asymmetric phyllosilicate particles hindered a full compaction of irregular porous refractory particles, generating a co-continuous two-phase microstructure. As the follicular phase (comprised of expanded phyllosilicate particles) and the granular one (containing hard-burnt MgO and calcitic dolomite particles and calcium silicate hydrates) intermeshed and bonded with the aid of a colloidal silica binder, a

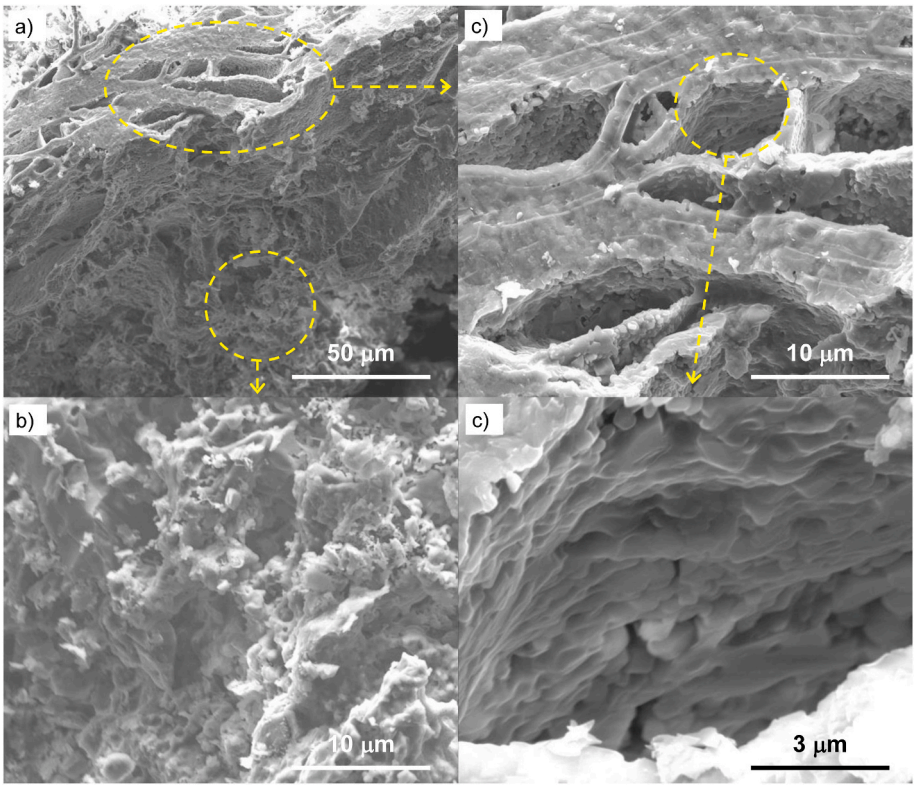

Fig. 11. SEM images of the cross-section of MPMB thermal insulator thermally treated at 1100 °C detailing the interface between follicular and granular phases.

structure of high total porosity and compression strength was attained. The two populations of micrometric and sub-micrometric pores formed after drying behaved effectively as sites for phonons scattering, reducing the material's thermal conductivity up to 600 °C. Between 600 and 1000 °C, besides the high total porosity levels, the presence of an opacifying agent (TiO_2) favored photon scattering, reducing even further the thermal conduction that occurred by irradiation of infrared waves. The formation of small portions of liquid phase above 800 °C did not affect the total porosity and pores size distribution significantly, since the high-refractoriness coarse particles formed a rigid structure that prevented loss of strength and shrinkage. Above 1100 °C, the presence of a larger amount of liquid modified the microstructure, particularly enhancing the average pore size and the ability to block heat flux. In comparison to other classes of insulators, such as ceramic-fiber blankets, the synergic combination of low thermal conductivity and high compression strength enabled the use of this novel material as self-supporting thinner insulating linings in steel ladles and runners, equipment for primary aluminum processing, petrochemical units, and cement kilns.

Acknowledgments

The authors acknowledge Brazilian Research Foundations FAPESP (2010-19274-5; 2017/06738-2; 2018/19773-3; 2022/03655-7), CNPq (305877/2017-8; 304081/2020-5; 150265/2022-0), and CAPES (Finance Code 001) for supporting this research, and the Electron Microscopy Laboratory of Advanced Materials Research Support Center (SMM/IFSC) for the SEM images. They declare that, to the best of their knowledge, no competing interests (financial or personal) affected the results reported in this paper and that they cited all funding and supporting sources.

References

[1] I. Nettleship, Applications of porous ceramics, Key Eng. Mater. (122–124) (1996) 305–324.
[2] A.R. Studart, U.T. Gonzenbach, E. Tervoort, L.J. Gauckler, Processing routes to macroporous ceramics: a review, J. Am. Ceram. Soc. 89 (6) (2006) 1771–1789, https://doi.org/10.1111/j.1551-2916.2006.01044.x.
[3] T. Ohji, M. Fukushima, Macro-porous ceramics: processing and properties, Int. Mater. Rev. 57 (2) (2012) 115–131, https://doi.org/10.1179/1743280411Y.0000000006.
[4] E.C. Hammel, O.L.-R. Ighodaro, O.I. Okoli, Processing and properties of advanced porous ceramics: an application based review, Ceram. Int. 40 (10) (2014) 15351–15370, https://doi.org/10.1016/j.ceramint.2014.06.095.
[5] R. Salomão, K.S. Oliveira, L. Fernandes, P. Tiba, U.S. Prado, Porous refractory ceramics for high-temperature thermal insulation - Part 1: the science behind energy saving, Interceram: Int.Ceram. Rev. 70 (3) (2021) 38–45, https://doi.org/10.1007/s42411-021-0460-1.
[6] R. Salomão, K. Oliveira, L. Fernandes, P. Tiba, U. Prado, Porous refractory ceramics for high-temperature thermal insulation - Part 2: the technology behind energy saving, Interceram: Int.Ceram. Rev. 71 (1) (2022) 38–50, https://doi.org/10.1007/s42411-022-0483-2.
[7] R. Salomão, L. Fernandes, U.S. Prado, P. Tiba, Porous refractory ceramics for high-temperature thermal insulation - Part 3: innovation in energy saving, Interceram: Int.Ceram. Rev. 71 (3) (2022) 30–37, https://doi.org/10.1007/s42411-022-0506-z.
[8] M. Fukushima, T. Ohji, Macroporous ceramics for the sustainable development goals (SDGs): review, Int. J. Appl. Ceram. Technol. 20 (2) (2023) 660–680, https://doi.org/10.1111/ijac.14261.
[9] R.L. Coble, W.D. Kingery, Effect of porosity on physical properties of sintered alumina, J. Am. Ceram. Soc. 39 (11) (1956) 377–385, https://doi.org/10.1111/j.1151-2916.1956.tb15608.x.
[10] E. Litovsky, M. Shapiro, A. Shavit, Gas pressure and temperature dependences of thermal conductivity of porous ceramic materials: Part 2, refractories and ceramics with porosity exceeding 30%, J. Am. Ceram. Soc. 79 (5) (1996) 1366–1376, https://doi.org/10.1111/j.1151-2916.1996.tb08598.x.
[11] V.A. Petrov, Combined radiation and conduction heat transfer in high temperature fiber thermal insulation, Int. J. Heat Mass Tran. 40 (9) (1997) 2241–2247, https://doi.org/10.1016/S0017-9310(96)00242-6.
[12] L. Braginsky, V. Shklover, H. Hofmann, P. Bowen, High-temperature thermal conductivity of porous Al_2O_3 nanostructures, art, Phys. Rev. B Condens. Matter 70 (13) (2004), 134201, https://doi.org/10.1103/PhysRevB.70.134201, 134201-1-134201-7.

[13] J. Ordonez-Miranda, J.J. Alvarado-Gil, Effect of the pore shape on the thermal conductivity of porous media, J. Mater. Sci. 47 (18) (2012) 6733–6740, https://doi.org/10.1007/s10853-012-6616-7.

[14] D.S. Smith, A. Alzina, J. Bourret, B. Nait-Ali, F. Pennec, N. Tessier-Doyen, K. Otsu, H. Matsubara, P. Elser, U.T. Gonzenbach, Thermal conductivity of porous materials, J. Mater. Res. 28 (17) (2013) 2260–2272, https://doi.org/10.1557/jmr.2013.179.

[15] D.O. Vivaldini, A.A.C. Mourão, V.R. Salvini, V.C. Pandolfelli, Review: fundamentals and materials for the microstructure design of high performance refractory thermal insulating, Cerâmica 60 (354) (2014) 297–309, https://doi.org/10.1590/S0366-69132014000200021.

[16] Y. Li, X. Yang, D. Liu, J. Chen, D. Zhang, Z. Wu, Permeability of the porous Al_2O_3 ceramic with bimodal pore size distribution, Ceram. Int. 45 (5) (2019) 5952–5957, https://doi.org/10.1016/j.ceramint.2018.12.064.

[17] D. Van Garsel, T.G. Swansinger, G. Routschka, New insulating raw material for high temperature applications, in: Proceedings of 41st International Colloquium on Refractories, 1998, pp. 122–128. Aachen, Germany.

[18] Z.-Y. Deng, T. Fukasawa, M. Ando, G.-J. Zhang, T. Ohji, Microstructure and mechanical properties of porous alumina ceramics fabricated by the decomposition of aluminum hydroxide, J. Am. Ceram. Soc. 84 (11) (2001) 2638–2644, https://doi.org/10.1111/j.1151-2916.2001.tb01065.x.

[19] A. Overhoff, A. Buhr, J. Grass, H.M. Wuthnow, New microporous materials, Ceram. Forum Int. 82 (8) (2005) 1–5.

[20] R. Kockegey-Lorenz, A. Buhr, R.P. Racher, Industrial application experiences with microporous calcium hexaluminate insulating material SLA-92, in: Proceedings of 48th International Colloquium on Refractories, 2005, pp. 66–70. Aachen, Germany.

[21] R. Salomão, M.O.C.V. Bôas, V.C. Pandolfelli, Porous alumina-spinel ceramics for high temperature applications, Ceram. Int. 37 (4) (2011) 1393–1399, https://doi.org/10.1016/j.ceramint.2011.01.012.

[22] Lightweight refractory can improve kiln insulation performance and fuel efficiency, Interceram. Int. Ceram. Rev. 69 (2020) 16–19, https://doi.org/10.1007/s42411-020-0108-6.

[23] R. Salomão, C.C. Arruda, V.C. Pandolfelli, L. Fernandes, Designing high-temperature thermal insulators based on densification-resistant in situ porous spinel, J. Eur. Ceram. Soc. 41 (4) (2021) 2923–2937, https://doi.org/10.1016/j.jeurceramsoc.2020.12.014.

[24] A. Gomez-Gomez, B. Winhard, E. Lilleodden, N. Huber, K.P. Furlan, Unraveling the role of shell thickness and pore size on the mechanical properties of ceramic-based macroporous structures, J. Am. Ceram. Soc. 106 (2) (2023) 1273–1286, https://doi.org/10.1111/jace.18811.

[25] E. Horie, Ceramic Fiber Insulation Theory and Practice, The Eibun Press Ltd, Osaka, Japan, 1987, pp. 25–87.

[26] H. Schmidt, D. Koch, G. Grathwohl, P. Colombo, Micro-/Macroporous ceramics from preceramic precursors, J. Am. Ceram. Soc. 84 (10) (2001) 2252–2255, https://doi.org/10.1111/j.1151-2916.2001.tb00997.x.

[27] P. Colombo, Conventional and novel processing methods for cellular ceramics, Phil. Trans. Math. Phys. Eng. Sci. 364 (2006) 109–124, https://doi.org/10.1098/rsta.2005.1683, 1838.

[28] U.T. Gonzenbach, A.R. Studart, D. Steinlin, E. Tervoort, L.J. Gauckler, Processing of particle-stabilized wet foams into porous ceramics, J. Am. Ceram. Soc. 90 (11) (2007) 3407–3414, https://doi.org/10.1111/j.1551-2916.2007.01907.x.

[29] W. Yan, J. Chen, N. Li, W. Qiu, Y. Wei, B. Han, Preparation and characterization of porous MgO-Al_2O_3 refractory aggregates using an in-situ decomposition pore-forming technique, Ceram. Int. 41 (1) (2015) 515–520, https://doi.org/10.1016/j.ceramint.2014.08.099.

[30] S.-H. Park, Types and health hazards of fibrous materials used as asbestos substitutes, Saf. Health Work 9 (3) (2018) 360–364, https://doi.org/10.1016/j.shaw.2018.05.001.

[31] S. Sobhani, S. Allan, P. Muhunthan, E. Boigne, M. Ihme, Additive manufacturing of tailored macroporous ceramic structures for high-temperature applications, Adv. Eng. Mater. 22 (8) (2020), 2000158, https://doi.org/10.1002/adem.202000158 art.

[32] M. Kaviany, Principles of Heat Transfer in Porous Media, second ed., Springer-Verlag, Germany, 1991, pp. 259–360.

[33] P.S. Sepulveda, N. Wilson, V.C. Pandolfelli, J.C. Bressiani, R. Taylor, Thermal conductivity of gelcast porous alumina, Am. Ceram. Soc. Bull. 78 (2) (1999) 61–66.

[34] Q. Zheng, W. Wang, Calcium silicate based high efficiency thermal insulation, Br. Ceram. Trans. 99 (4) (2000) 187–190, https://doi.org/10.1179/096797800680929.

[35] M.F. Modest, Radiative Heat Transfer, second ed., Academic Press, USA, 2003, pp. 58–149.

[36] T. Tritt, Thermal Conductivity: Theory, Properties, and Applications, first ed., Kluwer Academic, New York, USA, 2004, pp. 80–156.

[37] T.L. Bergman, A.S. Lavine, F.P. Incropera, D.P. DeWitt, Fundamentals of Heat and Mass Transfer, eighth ed., John Wiley & Sons, New York, 2011, pp. 50–85.

[38] E. Rathakrishnan, Elements of Heat Transfer, first ed., Taylor & Francis Group, 2012, pp. 45–91.

[39] E.S. Toberer, L.L. Baranowski, C. Dames, Advances in thermal conductivity, Annu. Rev. Mater. Res. 42 (2012) 179–209, https://doi.org/10.1146/annurev-matsci-070511-155040.

[40] T. Shimizu, K. Matsuura, H. Furue, K. Matsuzak, Thermal conductivity of high porosity alumina refractory bricks made by a slurry gelation and foaming method, J. Eur. Ceram. Soc. 33 (15–16) (2013) 3429–3435, https://doi.org/10.1016/j.jeurceramsoc.2013.07.001.

[41] R. Salomão, F.A. Cardoso, L.R.M. Bittencourt, Effect of polymeric fibers on refractory castable permeability, Am. Ceram. Soc. Bull. 82 (4) (2003) 51–56.

[42] C. Domínguez, J. Chevalier, R. Torrecillas, G. Fantozzi, Microstructure development in calcium hexaluminate, J. Eur. Ceram. Soc. 21 (3) (2001) 381–387, https://doi.org/10.1016/S0955-2219(00)00143-6.

[43] L. Fu, H. Gu, A. Huang, M. Zhang, X. Hong, L. Jin, Possible improvements of alumina-magnesia castable by lightweight microporous aggregates, Ceram. Int. 41 (1) (2015) 1263–1270, https://doi.org/10.1016/j.ceramint.2014.09.056.

[44] L.L. Sousa, A.D.V. Souza, L. Fernandes, V.L. Arantes, R. Salomão, Development of densification-resistant castable porous structures from in situ mullite, Ceram. Int. 41 (8) (2015) 9443–9454, https://doi.org/10.1016/j.ceramint.2015.03.328, art. no. 10407.

[45] M. Fukushima, Y.-I. Yoshizawa, Fabrication and morphology control of highly porous mullite thermal insulators prepared by gelation freezing route, J. Eur. Ceram. Soc. 36 (12) (2016) 2947–2953, https://doi.org/10.1016/j.jeurceramsoc.2015.09.041.

[46] L.M.M. Costa, J. Sakihama, R. Salomão, Characterization of porous calcium hexaluminate ceramics produced from calcined alumina and microspheres of Vaterite (μ-CaCO3), J. Eur. Ceram. Soc. 38 (15) (2018) 5208–5218, https://doi.org/10.1016/j.jeurceramsoc.2018.07.034.

[47] K. Pimraksa, P. Chindaprasirt, Lightweight bricks made of diatomaceous earth, lime and gypsum, Ceram. Int. 35 (1) (2009) 471–478, https://doi.org/10.1016/j.ceramint.2008.01.013.

[48] G. Jean, V. Sciamanna, M. Demuynck, F. Cambier, M. Gonon, Macroporous ceramics: novel route using partial sintering of alumina-powder agglomerates obtained by spray-drying, Ceram. Int. 40 (7) (2014) 10197–10203, https://doi.org/10.1016/j.ceramint.2014.02.089. PART A).

[49] R. Salomão, Porogenic behavior of water in high-alumina castable structures, Adv. Mater. Sci. Eng. (2018), 2876851, https://doi.org/10.1155/2018/2876851, 2018, art.

[50] M. Fukushima, Y.-I. Yoshizawa, T. Ohji, Macroporous ceramics by gelation-freezing route using gelatin, Adv. Eng. Mater. 16 (6) (2014) 607–620, https://doi.org/10.1002/adem.201400067.

[51] S. Vijayan, R. Narasimman, K. Prabhakaran, Freeze gelcasting of naphthalene-in-aqueous alumina slurry emulsions for the preparation of macroporous alumina ceramics, Ceram. Int. 41 (1) (2015) 1487–1494, https://doi.org/10.1016/j.ceramint.2014.09.083.

[52] P.P.R. Krishnan, P.A. Kumar, K. Prabhakaran, Preparation of macroporous alumina ceramics by ice templating without freeze drying using natural rubber latex binder, J. Porous Mater. (2023), https://doi.org/10.1007/s10934-023-01437-z.

[53] O. Lyckfeldt, J.M.F. Ferreira, Processing of porous ceramics by 'starch consolidation', J. Eur. Ceram. Soc. 18 (2) (1998) 131–140, https://doi.org/10.1016/s0955-2219(97)00101-5.

[54] A. Díaz, S. Hampshire, Characterisation of porous silicon nitride materials produced with starch, J. Eur. Ceram. Soc. 24 (2) (2004) 413–419, https://doi.org/10.1016/S0955-2219(03)00212-7.

[55] Z. Živcová, E. Gregorová, W. Pabst, D.S. Smith, A. Michot, C. Poulier, Thermal conductivity of porous alumina ceramics prepared using starch as a pore-forming agent, J. Eur. Ceram. Soc. 29 (3) (2009) 347–353, https://doi.org/10.1016/j.jeurceramsoc.2008.06.018.

[56] R. Salomão, J. Brandi, Macrostructures with hierarchical porosity produced from alumina-aluminum hydroxide-chitosan wet-spun fibers, Ceram. Int. 39 (7) (2013) 8227–8235, https://doi.org/10.1016/j.ceramint.2013.04.007.

[57] R. Salomão, P.H. Cardoso, J. Brandi, Gelcasting porous alumina beads of tailored shape and porosity, Ceram. Int. 40 (PB) (2014) 16595–16601, https://doi.org/10.1016/j.ceramint.2014.08.017.

[58] M.D.M. Innocentini, R. Salomão, C. Ribeiro, F.A. Cardoso, V.C. Pandolfelli, R. P. Rettore, L.R.M. Bittencourt, Permeability of fiber-containing refractory castables, Am. Ceram. Soc. Bull. 81 (7) (2002) 34–38.

[59] M.D.M. Innocentini, R. Salomão, C. Ribeiro, F.A. Cardoso, V.C. Pandolfelli, R. P. Rettore, L.R.M. Bittencourt, Permeability of fiber-containing refractory castables, Am. Ceram. Soc. Bull. 81 (8) (2002) 65–68.

[60] K. Sasahara, T. Hyodo, Y. Shimizu, M. Egashira, Macroporous and nanosized ceramic films prepared by modified sol-gel method with PMMA microsphere templates, J. Eur. Ceram. Soc. 24 (6) (2004) 1961–1967, https://doi.org/10.1016/S0955-2219(03)00518-1.

[61] S. Hashimoto, S. Honda, T. Hiramatsu, Y. Iwamoto, Fabrication of porous spinel ($MgAl_2O_4$) from porous alumina using a template method, Ceram. Int. 39 (2) (2013) 2077–2081, https://doi.org/10.1016/j.ceramint.2012.08.062.

[62] W.-Z. Huang, F. Lin, S.L. Lee, F.-T. Tao, K.-L. Tung, Fabrication of microporous polyamide selective layer on macroporous ceramic hollow fibers via direct interfacial polymerization for nanofiltration applications, J. Membr. Sci. 658 (2022), 120710, https://doi.org/10.1016/j.memsci.2022.120710 art.

[63] X. Deng, J. Wang, J. Liu, H. Zhang, L. Han, S. Zhang, Low cost foam-gelcasting preparation and characterization of porous magnesium aluminate spinel ($MgAl_2O_4$) ceramics, Ceram. Int. 42 (16) (2016) 18215–18222, https://doi.org/10.1016/j.ceramint.2016.08.145.

[64] W. Zhou, W. Yan, N. Li, Y. Li, Y. Dai, Z. Zhang, S. Ma, Fabrication of mullite-corundum foamed ceramics for thermal insulation and effect of micro-pore-foaming agent on their properties, J. Alloys Compd. 785 (2019) 1030–1037, https://doi.org/10.1016/j.jallcom.2019.01.212.

[65] A.L. Brooks, Z. Shen, H. Zhou, Development of a high-temperature inorganic synthetic foam with recycled fly-ash cenospheres for thermal insulation brick manufacturing, J. Clean. Prod. 246 (2020), 118748, https://doi.org/10.1016/j.jclepro.2019.118748 art.

[66] I.C. Finhana, O.H. Borges, T. Santos Jr., V.R. Salvini, V.C. Pandolfelli, Direct foaming of Al_2O_3-based macroporous ceramics containing pre-foamed colloidal alumina, calcite and CAC suspension, Ceram. Int. 47 (16) (2021) 22717–22724, https://doi.org/10.1016/j.ceramint.2021.04.287.

[67] I.C. Finhana, V.V.S. Machado, T. Santos Jr., O.H. Borges, V.R. Salvini, V. C. Pandolfelli, Direct foaming of macroporous ceramics containing colloidal alumina, Ceram. Int. 47 (11) (2021) 15237–15244, https://doi.org/10.1016/j.ceramint.2021.02.086.

[68] A. Shimamura, A review on gradient macroporous ceramic via powder-based direct foaming process, J. Ceram. Soc. Jpn. 130 (2) (2022) 204–210, https://doi.org/10.2109/JCERSJ2.21061.

[69] A.D.V. Souza, L.L. Sousa, L. Fernandes, P.H.L. Cardoso, R. Salomão, Al_2O_3-Al$(OH)_3$-Based castable porous structures, J. Eur. Ceram. Soc. 35 (6) (2015) 1943–1954, https://doi.org/10.1016/j.jeurceramsoc.2015.01.003.

[70] A.D.V. Souza, R. Salomão, Evaluation of the porogenic behavior of aluminum hydroxide particles of different size distributions in castable high-alumina structures, J. Eur. Ceram. Soc. 36 (3) (2016) 885–897, https://doi.org/10.1016/j.jeurceramsoc.2015.11.019.

[71] R. Salomão, L. Fernandes, Porous co-continuous mullite structures obtained from sintered aluminum hydroxide and synthetic amorphous silica, J. Eur. Ceram. Soc. 37 (8) (2017) 2849–2856, https://doi.org/10.1016/j.jeurceramsoc.2017.03.017.

[72] M. Fujiwara, K. Shiokawa, I. Sakakura, Y. Nakahara, Silica hollow spheres with nano-macroholes like diatomaceous earth, Nano Lett. 6 (12) (2006) 2925–2928, https://doi.org/10.1021/nl062298i.

[73] F. Akhtar, Y. Rehman, L. Bergström, A study of the sintering of diatomaceous earth to produce porous ceramic monoliths with bimodal porosity and high strength, Powder Technol. 201 (3) (2010) 253–257, https://doi.org/10.1016/j.powtec.2010.04.004.

[74] L. Xu, Y. Jiang, J. Feng, J. Feng, C. Yue, Infrared-opacified Al_2O_3-SiO_2 aerogel composites reinforced by SiC-coated mullite fibers for thermal insulations, Ceram. Int. 41 (1) (2015) 437–442, https://doi.org/10.1016/j.ceramint.2014.08.088.

[75] L.L. Sousa, R. Salomão, V.L. Arantes, Development and characterization of porous moldable refractory structures of the alumina-mullite-quartz system, Ceram. Int. 43 (1) (2017) 1362–1370, https://doi.org/10.1016/j.ceramint.2016.10.093.

[76] L. Fernandes, R. Salomão, Preparation and characterization of mullite-alumina structures formed "in situ" from calcined alumina and different grades of synthetic amorphous silica, Mater. Res. 21 (3) (2018), e20170783, https://doi.org/10.1590/1980-5373-MR-2017-0783 art.

[77] H. Chen, L. Zhao, X. He, W. Fang, Z.-X. Lei, H. Chen, The fabrication of porous corundum spheres with core-shell structure for corundum-spinel castables, Mater. Des. 85 (2015) 574–581, https://doi.org/10.1016/j.matdes.2015.07.033.

[78] W. Yan, X. Lin, J. Chen, N. Li, Y. Wei, B. Han, Effect of TiO_2 addition on microstructure and strength of porous spinel ($MgAl_2O_4$) ceramics prepared from magnesite and $Al(OH)_3$, J. Alloys Compd. 618 (2015) 287–291, https://doi.org/10.1016/j.jallcom.2014.08.169.

[79] F. Wang, J. Ye, G. He, G. Liu, Z. Xie, J. Li, Preparation and characterization of porous $MgAl_2O_4$ spinel ceramic supports from bauxite and magnesite, Ceram. Int. 41 (6) (2015) 7374–7380, https://doi.org/10.1016/j.ceramint.2015.02.044.

[80] X. Lin, W. Yan, N. Li, Phase composition and pore evolution of porous periclase-spinel ceramics prepared from magnesite and Al(OH)3, Sci. Sinter. 48 (2) (2016) 147–155, https://doi.org/10.2298/SOS1602147L.

[81] G. Wu, W. Yan, S. Schafföner, X. Lin, S. Ma, Y. Zhai, X. Liu, L. Xu, Effect of magnesium aluminate spinel content of porous aggregates on cement clinker corrosion and adherence properties of lightweight periclase-spinel refractories, Construct. Build. Mater. 185 (2018) 102–109, https://doi.org/10.1016/j.conbuildmat.2018.07.058.

[82] I.R. de Oliveira, V.M.C. Leite, M.P.V.P. Lima, R. Salomão, Production of porous ceramic material using different sources of alumina and calcia, Rev. Mater. 20 (3) (2015) 739–746, https://doi.org/10.1590/S1517-707620150003.0078.

[83] R. Salomão, V.L. Ferreira, L.M.M. Costa, I.R. de Oliveira, Effects of the initial CaO-Al_2O_3 ratio on the microstructure development and mechanical properties of porous calcium hexaluminate, Ceram. Int. 44 (2) (2018) 2626–2631, https://doi.org/10.1016/j.ceramint.2017.11.010.

[84] O.H. Borges, T. Santos Jr., V.R. Salvini, V.C. Pandolfelli, Al_2O_3–CaO macroporous ceramics containing hydrocalumite-like phases, Ceram. Int. 46 (5) (2020) 5929–5936, https://doi.org/10.1016/j.ceramint.2019.11.046.

[85] M.D.M. Innocentini, C. Ribeiro, R. Salomão, V.C. Pandolfelli, L.R.M. Bittencourt, Assessment of mass loss and permeability changes during the dewatering process of refractory castables containing polypropylene fibers, J. Am. Ceram. Soc. 85 (8) (2002) 2110–2112, https://doi.org/10.1111/j.1151-2916.2002.tb00413.x.

[86] R. Salomão, M.A. Kawamura, A.B.V. Emilio, J. Sakihama, A.M. Segadães, Calcium aluminate cement in castable alumina: from hydrate bonding to the in situ formation of calcium hexaluminate, Ceram. Int. 47 (11) (2021) 15082–15093, https://doi.org/10.1016/j.ceramint.2021.02.066.

[87] B. Guene Lougou, L. Wu, D. Ma, B. Geng, B. Jiang, D. Han, H. Zhang, P. Łapka, Y. Shuai, Efficient conversion of solar energy through a macroporous ceramic receiver coupling heat transfer and thermochemical reactions, Energy 271 (2023), https://doi.org/10.1016/j.energy.2023.126989 art. no. 126989.

[88] I.R. Oliveira, R. Salomão, V.C. Pandolfelli, A.R. Studart, High-carbon-content refractory castables, Am. Ceram. Soc. Bull. 82 (10) (2003) 8.

[89] R. Salomão, C.C. Arruda, M.L.P. Antunes, Synthesis, dehydroxylation and sintering of porous $Mg(OH)_2$-MgO clusters: evolution of microstructure and physical properties, Interceram: Int.Ceram. Rev. 69 (1) (2020) 52–62, https://doi.org/10.1007/s42411-019-0067-y.

[90] V.T. Shmuradko, F.I. Panteleenko, O.P. Reut, E.F. Panteleenko, N.V. Kirshina, Composition, structure, and property formation of heat insulation fire- and heat-reflecting materials based on vermiculite for industrial power generation, Refract. Ind. Ceram. 53 (4) (2012) 254–258, https://doi.org/10.1007/s11148-012-9503-5.

[91] S.A. Suvorov, V.V. Skurikhin, Vermiculite - a promising material for high-temperature heat insulators, Refract. Ind. Ceram. 44 (3) (2003) 186–193, https://doi.org/10.1023/A:1026312619843.

[92] T.D. Ciach, J.E. Gillott, E.G. Swenson, P.J. Sereda, Microstructure of calcium silicate hydrates, Cement Concr. Res. 1 (1) (1971) 13–25, https://doi.org/10.1016/0008-8846(71)90080-9.

[93] K. Lin, J. Chang, Y. Zeng, W. Qian, Preparation of macroporous calcium silicate ceramics, Mater. Lett. 58 (15) (2004) 2109–2113, https://doi.org/10.1016/j.matlet.2004.01.008.

[94] I.G. Richardson, The calcium silicate hydrates, Cement Concr. Res. 38 (2) (2008) 137–158, https://doi.org/10.1016/j.cemconres.2007.11.005.

[95] R. Salomão, V.C. Pandolfelli, Microsilica addition as an antihydration technique for magnesia-containing refractory castables, Am. Ceram. Soc. Bull. 86 (6) (2007) 9301–9309.

[96] R. Salomão, I.S. Martinatti, L. Fernandes, A. Sundblom, P. Greenwood, P.R. T. Tiba, Novel silanized colloidal silica-MgO self-flowing dispersions with improved hydroxylation resistance, J. Eur. Ceram. Soc. 43 (13) (2023) 5691–5705, https://doi.org/10.1016/j.jeurceramsoc.2023.05.023.

[97] R. Salomão, I.S. Martinatti, L. Fernandes, S. Andreas, P. Greenwood, P.R.T. Tiba, Novel colloidal silica technology for MgO-containing refractories – Part 1: anti-hydroxylation binder, Open Ceram. 15 (2023), 100397, https://doi.org/10.1016/j.oceram.2023.100397.

[98] S. Banerjee, Recent developments in monolithic refractories, Am. Ceram. Soc. Bull. 77 (10) (1998) 59–63.

[99] M.R. Ismael, R. Salomão, V.C. Pandolfelli, Refractory castables based on colloidal silica and hydratable alumina, Am. Ceram. Soc. Bull. 86 (9) (2007) 58–61.

[100] R.P.S. Chakradhar, B.M. Nagabhushana, G.T. Chandrappa, K.P. Ramesh, J.L. Rao, Solution combustion derived nanocrystalline macroporous wollastonite ceramics, Mater. Chem. Phys. 95 (1) (2006) 169–175, https://doi.org/10.1016/j.matchemphys.2005.06.002.

[101] Y. Ma, J. Li, X. Wang, L. Liu, C. Wang, Highly permeable macroporous cordierite ceramics with controlled microstructure produced by particle-stabilized emulsions with a reactive thermal treatment, J. Eur. Ceram. Soc. 37 (9) (2017) 3203–3211, https://doi.org/10.1016/j.jeurceramsoc.2017.03.035.

[102] A.I. Zaitsev, A.D. Litvina, N.P. Lyakishev, B.M. Mogutnov, Thermodynamics of CaO-Al_2O_3-SiO_2 and CaF_2-CaO-Al_2O_3-SiO_2 melts, J. Chem. Soc., Faraday Trans. 93 (1997) 3089–3098, https://doi.org/10.1039/A700511C.